

Prospects of detecting gamma-ray emission from galaxy clusters: cosmic rays and dark matter annihilations

Anders Pinzke^{1,*}, Christoph Pfrommer^{2,†} and Lars Bergström^{3,‡}

¹*University of California - Santa Barbara, Department of Physics, CA 93106-9530, USA*

²*Heidelberg Institute for Theoretical Studies (HITS),*

Schloss-Wolfsbrunnengasse 33, DE - 69118 Heidelberg, Germany and

³*The Oskar Klein Centre for Cosmoparticle Physics, Department of Physics, Stockholm University, AlbaNova University Center, SE - 106 91 Stockholm, Sweden*

(Dated: March 28, 2011)

... to be written...

PACS numbers: 95.35.+d, 95.85.Pw, 98.62.Gq, 98.65.-r, 98.70.Sa

I. INTRODUCTION

Dark matter has been searched for in direct detection experiments [1], at accelerators [2–4] and also in indirect detection experiments looking for signals in the cosmic-ray spectra of antiprotons, positrons, neutrinos and all of the electromagnetic spectrum from radio waves to gamma rays [5]. So far, the improvements in direct detection sensitivity have put this method into focus, but the situation may change considerably the coming few years as the CERN LHC experiments collect data, and new gamma-ray detectors are being planned, such as the CTA [6]. In fact, it has recently been pointed out [7] that a dedicated ground-based gamma-ray detector would have potential that goes far beyond that of the other methods, depending on presently unknown parameters in the particle physics models for dark matter.

Among the astrophysical systems which will be very interesting to detect, and study, with coming gamma-ray detectors (Fermi, HESS, MAGIC, VERITAS, and eventually large detectors like CTA) belong galaxy clusters. The most promising directions in which to search for a gamma-ray annihilation signal (from the annihilation process itself, and also the accompanying bremsstrahlung and inverse Compton components coming from charged particles produce in the annihilations) are basically three:

1. The galactic centre (g.c.). This is where all numerical simulations of cold dark matter predict the highest density. However, the detailed dark matter density in the very central part is difficult to predict, due to a possibly very complicated interplay between baryons, dark matter, and the central galactic black hole. Also, it is a very crowded region with many gamma-ray sources like pulsars and other supernova remnants, which have to be subtracted from the data to extract the dark matter induced signal. In fact, there is a recent claim of an indication of a relatively light dark matter particle contribution to the gamma-ray flux from the g.c. [8], but other hypotheses seem to work at least as well [9].

2. The dwarf spheroidal galaxies orbiting the Milky Way, like Segue-1, Ursa Minor, Draco, Sagittarius, Sculptor, Carina or Willman-1 [10–12]. The problem here is that the nature of many of these small, dark matter-dominated galaxies is not entirely clear, and the velocity dispersion estimates are based on rather small numbers of stars. Tidal disruption and confusion with star clusters are other complications. Thus the dark matter density profile is very uncertain for most of them. Nonetheless, by stacking the data together from many dwarf spheroidals these uncertainties can be made less severe, and preliminary results from Fermi-LAT shows this method to give quite promising results [13].

3. Galaxy clusters. This possibility has been less studied, however we noted in a previous Letter [14] that there are certain advantages that work in favour of this possible target for gamma-ray detection of dark matter annihilation. Galaxy clusters constitute the most massive objects in our Universe that are forming today. This causes their DM subhalo mass function to be less affected by tidal stripping compared to galaxy sized halos that formed long ago. The annihilation luminosities of the DM halo component for e.g. the Virgo cluster and the Draco dwarf scales in a way (see [14]) that the ratio of gamma-ray luminosities from the smooth components is around 4, in favour of Virgo. In addition, there may be a further enhancement due to substructure, which to a large extent should be unaffected by tidal disruption, at least in the outer regions. According to a recent estimate [15], more massive haloes tend to have a larger mass fraction in subhalos. For example, cluster size haloes typically have 7.5 per cent of the mass within r_{200} in substructures of fractional mass larger than 10^{-5} , which is 25 per cent higher than galactic haloes [16].

For a satellite dwarf galaxy, however, once it is accreted by the Milky Way, the outer regions are severely affected by tidal stripping. The longer a satellite has been part of our Galaxy, and the closer it comes to the center during its pericentral passage, the more material is removed [17].

In this paper, we will investigate in some more detail the potential of several of the most promising galaxy clusters to yield an annihilation gamma-ray yield which could be observable with present and planned gamma-ray detectors.

* apinzke@physics.ucsb.edu

† pfrommer@cita.utoronto.ca

‡ lbe@fysik.su.se

For previous work related to dark matter in clusters, see, e.g., [18, 19].

Anders, insert your flux table for various clusters, and discuss it

This yields Fornax ($M_{200} = 10^{14} M_{\odot}$) and Virgo ($M_{200} = 2.1 \times 10^{14} M_{\odot}$) as the prime targets for DM observations, Perseus ($M_{200} = 7.7 \times 10^{14} M_{\odot}$) for CR induced emission and we additionally decide in favor of the well studied cluster Coma ($M_{200} = 1.4 \times 10^{15} M_{\odot}$) for comparison.

II. THEORY

A. Astrophysics

The differential photon flux within a given solid angle $\Delta\Omega$ along a line-of-sight (los) is given by

$$\frac{dF_{\gamma}}{dE_{\gamma}} \equiv \frac{d^3 N_{\gamma}}{dA dt dE_{\gamma}} = \frac{1}{2} \int_{\Delta\Omega} d\psi \sin \psi \frac{dS_{\gamma}}{dE_{\gamma}}(\psi, E_{\gamma}), \quad (1)$$

where

$$\frac{dS_{\gamma}}{dE_{\gamma}}(\psi, E_{\gamma}) = \int_{\Delta\Omega} d\Omega \int_{\text{los}} dl q_{\text{sum}}(E_{\gamma}, r) \Lambda(\theta), \quad (2)$$

and $S_{\gamma}(\psi, > E_{\gamma})$ denotes the surface brightness above the photon energy E_{γ} . The integration along the line-of-sight l , in the direction ψ that the detector is pointing, is parameterized such that the radius of the source $r = \sqrt{l^2 + D^2 - 2Dl \cos \Psi}$, where D is the distance to the source from the galactic center and $\cos \Psi \equiv \cos \theta \cos \psi - \cos \varphi \sin \theta \sin \psi$. The angular integration $d\Omega = \sin \theta d\theta d\varphi$ is performed over a cone centered around ψ and the opening angle $\Delta\Omega$ is typically taken to be a few times the point spread function (PSF) θ_{res} . The limited angular resolution results in a probability that a photon coming from a direction ψ' is instead reconstructed to a direction ψ , where the underlying probability distribution follow a Gaussian:

$$\Lambda(\theta) = \frac{1}{2\pi\theta_{\text{res}}^2} \exp \left[-\frac{\theta^2}{2\theta_{\text{res}}^2} \right], \quad \text{where } \theta = \psi' - \psi. \quad (3)$$

We denote the total source function by $q_{\text{sum}}(E_{\gamma}, r)$, where we include contributions from five main processes; leptophilic DM annihilating to μ^+/μ^- decaying to e^+/e^- pairs that up-scatter background photons (IC), leptophilic DM emitting final state radiation (FSR), DM benchmark models where neutralino annihilations generate electrons that up-scatter background photons (BM-IC) and emit a continuum as well as final state radiation (BM-Cont), and CR induced π^0 :s decaying into gamma-rays. The source function is given by

$$q_{\text{sum}}(E_{\gamma}, r) = q_{\pi^0-\gamma}(E_{\gamma}, r) + \sum_i q_{\text{sm},i}(E_{\gamma}, r) B_{\text{tot},i}(\sigma_v, r) \quad (4)$$

where the subscript i runs over the gamma-ray producing DM channels. The differential CR to gamma-ray source function is denoted by $q_{\pi^0-\gamma}(E_{\gamma}, r)$, where we refer the reader to Sect. II A 2 and [20] for further details. The total differential boost factor for DM is the product of enhancement factors from SFE $B_{\text{sfe}}(\sigma_v)$ (see Sect. II B 1) and from substructure enhancement over the smooth halo contribution $B_{\text{sub},i}(r) = 1 + q_{\text{sub}}(r)/q_{\text{sm},i}(r)$ (see Sect. II A 1) and is denoted by $B_{\text{tot},i}(r, \sigma_v) = B_{\text{sfe}}(\sigma_v) B_{\text{sub},i}(r)$. The DM source function from the smooth halo for each process is written on the form:

$$q_{\text{sm},i}(E_{\gamma}, r) = \sum_j \frac{dN_{\gamma,j}}{dE_{\gamma}} \Gamma_j(r). \quad (5)$$

Here the annihilation rate density is given by

$$\Gamma_j(r) = \frac{1}{2} \left(\frac{\rho(r)}{m_{\chi}} \right)^2 \langle \sigma v \rangle_j \quad (6)$$

where the subscript j runs over all kinematically allowed gamma-ray producing channels each with the spectrum $\frac{dN_{\gamma,j}}{dE_{\gamma}}$ and annihilation cross-section $\langle \sigma v \rangle_j$. We denote the DM mass with m_{χ} and the DM density profile with $\rho(r)$. Typically the universal Navarro-Frenk-White (NFW) density profile provide a good fit to both the observed and simulated clusters. It can be considered as a special case of the 5-parameter profile:

$$\rho(r) = \frac{\rho_s}{(r/r_s + 1)^{\gamma} [1 + (r/r_s)^{\delta}]^{\delta}}, \quad \delta = \frac{\beta - \gamma}{\alpha}, \quad (7)$$

where a cuspy NFW profile is given by $(\alpha, \beta, \gamma) = (1, 3, 1)$. The scaling radius is given by r_s and the characteristic density by $\rho_s = (\Delta\rho_c/3) c^3 / (\log(1+c) - (c/(1+c)))$, where the halo mass dependent concentration parameter c is derived from a power-law fit to cosmological simulations with $M_{200} \gtrsim 10^{10} M_{\odot}$ [21],

$$c = 3.56 \times \left(\frac{M_{200}}{10^{15} M_{\odot}} \right)^{-0.098}. \quad (8)$$

This mass scaling agrees well with [22] for cluster-mass halos after converting the concentration definitions according to [23]. In this work we choose to model the DM density by an Einasto density profile

$$\rho_{\text{ein}}(r) = \rho_{-2} \exp \left\{ -\frac{2}{\alpha} \left[\left(\frac{r}{r_{-2}} \right)^{\alpha} - 1 \right] \right\}, \quad \alpha = 0.17, \quad (9)$$

that is slightly shallower in the center than the conventional Navarro-Frenk-White (NFW) profile, but provide a better fit to simulated DM halos [24]. We denote the density where the profile has a slope of -2 by ρ_{-2} , and the radius by r_{-2} . Assuming that all the flux from an NFW profile originate from within the scale radius $r_s = r_{200}/c$, and all the flux from an Einasto profile originate within $r_{-2} = r_{200}/c$, it follows that $\rho_{-2} = \rho_s/4$. The virial radius r_{200} of a halo is defined to be the radius at which the mean density within is a factor $\Delta = 200$ times the critical density ρ_c of the universe.

1. Substructures

High-resolution DM only simulations of Milky Way (MW) type halos find substantial amount of substructures in the periphery of DM halos, while the substructures in the center are erased due to dynamical disruption. Since the rate of which DM is annihilating depends on the density squared, the resulting flux is boosted compared to the smooth density distribution. Recent simulations suggest a flux enhancement from substructures of the order of ten up to a few 100 [25, 26] for a MW size halo. Using the Aquarius simulations [27], we fit [28] to the luminosity from smooth substructures (i.e. substructures within substructures are not included) inside radius r . The best fit is given by

$$L_{\text{sub}}(< r) = 0.76 C_1 C_2(M_{200}) L_{200\text{sm}} x^{0.95} x^{-0.27}, \quad (10)$$

where $L_{200\text{sm}}$ is the luminosity from the smooth halo without substructures within r_{200} and $x = \left(\frac{r}{r_{200}}\right)$. The first normalization constant is derived from the simulations:

$$C_1 = \left(\frac{M_{\text{res,sim}}}{M_{\text{lim}}}\right)^{0.226}, \quad (11)$$

where $M_{\text{res,sim}} = 10^5 M_\odot$ is the minimum subhalo mass in the MW simulation, and M_{lim} the free streaming mass. Here we assume that the power-law scaling relation in Eq. (11) is valid down to the minimum mass of DM halos, which is conventionally in the cold dark matter universe [29, 30] taken to be $10^{-6} M_\odot$. Note that potentially the power-law could flatten towards smaller mass scales although current simulations show no hits of such a behavior and in addition we are approaching the asymptotic behavior in the power spectrum on these scales (CHECK). For DM halos more (less) massive than the MW we expect a larger (smaller) boost from substructures, simply because of the larger (smaller) mass range down to the minimum mass M_{lim} . We capture this halo mass dependence with the second normalization in Eq. (10):

$$C_2(M_{200}) = \left(\frac{M_{200}}{M_{200\text{sim}}}\right)^{0.226}, \quad (12)$$

where $M_{200\text{sim}} = 1.9 \times 10^{12} M_\odot$ is the mass of the MW halo in the simulation [27].

Recent detailed galaxy cluster observations find a core like density profile with an inner slope of $\beta = 0.6$, where $\beta \gtrsim 1$ can be ruled out to a $> 95\%$ confidence [31]. This finding is hard to reconcile with simulations that typically prefer a steeper central profile. The different density profiles have a large impact on the luminosity from annihilating DM, although the details of the density profile can be neglected compared to the dominating boost from substructures. In Fig. 1 we compare the radial dependence of the accumulative luminosity from different smooth cluster density profiles to the substructure

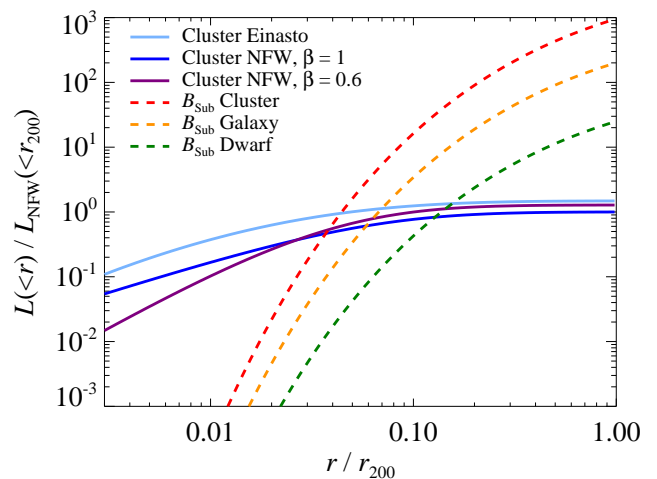


FIG. 1. Radial dependence of various luminosity contributions. The solid lines show the accumulative smooth luminosity from a cluster with the mass $M_{200} = 10^{15} M_\odot$ for three different density profiles; an Einasto profile with $\alpha = 0.17$ (light blue), a cuspy NFW profile with $\beta = 1.0$ (dark blue), and a core NFW profile with $\beta = 0.6$ (purple). The dashed lines show the accumulative luminosity from substructures for three different mass scales; an $M_{200} = 10^{15} M_\odot$ galaxy cluster (red), an $M_{200} = 10^{12} M_\odot$ galaxy (orange), and an $M_{200} = 10^8 M_\odot$ dwarf galaxy (green). All luminosities have been normalized with the luminosity within r_{200} from a cuspy NFW profile. We have assumed the standard value for the limiting substructure mass of $10^{-6} M_\odot$. Note the large expected boost from substructures in clusters (~ 1000), and the relative small boost in dwarf galaxies (~ 20).

boosted luminosity at different mass scales. We recalculate the density contrast for the core like density profile ρ_s and rescale the concentration parameter in Eq. (8) with 300/160 [31] to account for the more centralized scale radius in a core like cluster. The emission coming from the core compared to a cuspy like density profile is about 30% larger within r_{200} . This difference is build up within 10% of r_{200} (i.e. close to r_s). The emission from an Einasto density profile is about 50% larger than the cuspy NFW profile in the periphery of the cluster, where the difference is mainly build up at a few percent of r_{200} . The substructure boosted luminosities is negligible in the center of halos, but integrated out to r_{200} the boost is about; 10 for dwarf galaxies, 10^2 for galaxies, and 10^3 for galaxy clusters.

Even though the bulk of substructures have been erased in the central regions of DM halos, a cluster in projection has a significant enhancement due to substructures at a radius of just a few percent of r_{200} . In Fig. 2 we show the luminosity dominating radius for substructures and smooth density profiles, both for three different mass scales. It clearly shows how that the main contribution from the substructures is coming from outer parts of the DM halos, while the main contribution from the smooth density profiles peaks around the

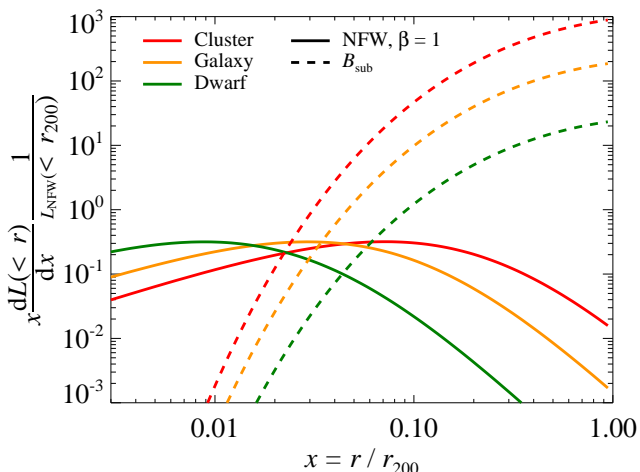


FIG. 2. Radial dependence of differential luminosity at different mass scales. The solid lines show the emissivity from a cuspy $\beta = 1.0$ NFW density profile for three different mass scales; an $M_{200} = 10^{15} M_{\odot}$ galaxy cluster (red), an $M_{200} = 10^{12} M_{\odot}$ galaxy (orange), and an $M_{200} = 10^8 M_{\odot}$ dwarf galaxy (green). The dashed lines show the emissivity from substructures for the same three mass scales. All emissivities have been normalized with the luminosity within r_{200} from a cuspy NFW profile. We have assumed the standard value for the limiting substructure mass of $10^{-6} M_{\odot}$.

scale radius. NOT QUITE, ALSO FIGURE IS SHOWING DIFF VOLUME, FAC 3 DIFFERENCE, WHAT DO WE REALLY LEARN FROM THE FIGURE

2. Cosmic-ray induced gamma-ray emission

The formation process of a galaxy cluster is a very energetic processes that induces both turbulence as well as frequently occurring merging and accretion shocks. These processes are thought to accelerate large quantities of relativistic non-thermal electrons and protons to high energies. On smaller scales, such as galaxies, there is convincing evidence of such non-thermal populations. Especially, in the MW, the cosmic rays are observed directly as well as indirectly through radio, X-ray, and gamma-ray emission. On larger scales of the order of few 100 kpc up to Mpc, there are a vast number of observations of radio emission coming from radio mini halos in the center of cooling flow clusters, radio relics in the periphery of clusters [32] as well smooth giant radio halos that have been observed in more than 50 clusters [33, 34]. Most of this observed radio emission is expected to emerge from synchrotron emitting cosmic-ray electrons whose precise origin in especially relics and giant radio halos is still not settled. However, due to the smoothness of the extended emission and the observed power-law slope it seems quite natural that they are of hadronic origin. Especially since the long cooling time of cosmic ray protons (CRs) allows for both an extended and large population of CRs

to build up over the cluster history [35].

When the CRs interact with ambient gas protons, it results in the production of both charged and neutral pions that decay into electrons, neutrinos, and gamma-rays. The production of these secondaries depend both on the gas and CR densities in the cluster, where the CR density roughly trace the gas outside the core regime and is slightly enhance in the center. This density scaling implies that clusters are great targets for Cherenkov telescopes with a high sensitivity for the central parts of close by clusters. Detecting the cluster gamma-ray emission is crucial in this respect as it potentially provides the unique and unambiguous evidence of CR populations in clusters through observing the π^0 bump at about 100 MeV in the spectra.

We adopt the spectrally and spatially universal gamma-ray model developed by Pinzke & Pfrommer [20] to estimate the emission from decaying π^0 :s that dominates over the inverse Compton emission from primary and secondary electrons above 100 MeV in clusters. The gamma-ray formalism was derived from high resolution simulations of clusters of galaxies that included radiative hydrodynamics, star formation, supernova feedback, and followed CR physics using a novel formulation that trace the most important injection and loss processes self-consistently while accounting for the CR pressure in the equation of motion [36–38]. We note that the overall normalization of the CR and gamma-ray distribution scales with the maximum acceleration efficiency at structure formation shock waves. Following recent observations at supernova remnants [39] as well as theoretical studies [40], we adopt a realistic value of this parameter and assume that 50% of the dissipated energy at strong shocks is injected into CRs while this efficiency rapidly decreases for weaker shocks [37].

B. Particle physics

1. Leptophilic models

Sommerfeld enhancement, electron spectra

2. Supersymmetric dark matter

neutralino, benchmark models, continuum emission, electron spectra

3. Final state radiation

The photon spectrum from resulting from FSR is universal with only a weak dependence of the underlying particle physics model. The photon yield from this pro-

cess is given by (see e.g. [41])

$$\frac{dN_{X\bar{X}}}{dx} \approx \frac{\alpha Q_X^2}{\pi} \mathcal{F}_X(x) \log \left[\frac{4m_X^2(1-x)}{m_X^2} \right]. \quad (13)$$

Here, the normalized photon energy $x = E_\gamma/m_\chi c^2$, $\alpha = e^2/\hbar c$ is the fine-structure constant, Q_X^2 and m_X the charge and mass of the particle X , respectively. The function $\mathcal{F}_X(x)$ depends on the spin of the final state and is given by

$$\mathcal{F}_{\text{fermion}}(x) = \frac{1 + (1-x)^2}{x} \quad (14)$$

for fermions.

C. Radiative processes

In this section we outline the basics of inverse Compton (IC) emission. As target radiation fields we consider both cosmic microwave background (CMB) photons, and the light from stars and dust (SD). We derive a semi-analytic model from which we can estimate the SD spectral and spatial distributions as a simple function of cluster mass.

1. Inverse Compton

The standard IC source function is given by [42]:

$$q_{\text{IC}}(E_\gamma, r) = \frac{d^3 N_\gamma}{dV dt dE_\gamma} = \frac{3}{4} c \sigma_T \int dE_{\text{ph}} \frac{n_{\text{ph}}(E_{\text{ph}})}{E_{\text{ph}}} \times \int dE_e \frac{dn_e}{dE_e}(E_e, r) \frac{(m_e c^2)^2}{E_e^2} G(\Gamma_e, q), \quad (15)$$

where E_e is the energy of the upscattering electrons and E_{ph} is the energy of the background photon field. We represent the Thomson cross-section with σ_T and the full differential Klein-Nishina (KN) cross-section is captured by [43]:

$$G(\Gamma_e, q) = 2q \ln q + (1+2q)(1-q) + \frac{1}{2} \frac{(\Gamma_e q)^2 (1-q)}{1 + \Gamma_e q}, \quad (16)$$

where

$$\Gamma_e = \frac{4E_{\text{ph}}E_e}{(m_e c^2)^2}, \quad \text{and} \quad q = \frac{E_\gamma}{\Gamma_e(E_e - E_\gamma)}. \quad (17)$$

The full KN cross-section accounts for the less efficient energy transfer between the photon and electron and results in a steepening of the IC gamma-ray spectrum. In the low energy Thomson regime the IC spectrum is given by $E_\gamma^{-(\alpha_e-1)/2}$, however when $\Gamma_e \gg 1$ the IC spectrum steepens due to the KN suppression to $E_\gamma^{-\alpha_e} \log(E_\gamma)$.

We account for two major contributions to the number density of radiative background fields n_{ph} ; the cosmic microwave background (CMB) photons and the infra-red (IR) to ultra-violet (UV) light emitted by starlight and dust (SD). The number density for the SD is given by $n_{\text{ph}} \equiv \frac{d^2 N_{\text{ph}}}{dV dE_{\text{ph}}}(E_{\text{ph}}, r) = \frac{u_{\text{SD}}(E_{\text{ph}}, r)}{E_{\text{ph}}^2}$ where the SD energy density $u_{\text{SD}}(E_{\text{ph}}, r)$ is given in Eq. (37). We model the CMB photon spectrum as a photon gas that is isotropically distributed and follows a black body spectrum with the temperature $T = 2.73$ K:

$$n_{\text{ph}}(E_{\text{ph}}) = \frac{d^2 N_{\text{ph}}}{dV dE_{\text{ph}}} = \frac{1}{\pi^2 (\hbar c)^3} \frac{E_{\text{ph}}^2}{\exp(E_{\text{ph}}/k_B T) - 1}. \quad (18)$$

Note that the typical energy of a black body photon before scattering is given by $\langle E_{\text{ph}} \rangle = \epsilon_{\text{ph}}/\tilde{n}_{\text{ph}} \approx 2.70 k_B T$, where \tilde{n}_{ph} and ϵ_{ph} are the number- and energy-density derived by integrating $n_{\text{ph}}(E_{\text{ph}})$ and $E_{\text{ph}} n_{\text{ph}}(E_{\text{ph}})$ over the photon energy E_{ph} , respectively.

The electrons injected from annihilating DM also suffer from diffusive and radiative losses. Hence we have to calculate the equilibrium spectrum of the electrons plus positrons denoted by $\frac{dn_e}{dE_e}$ in Eq. (15). We derive this stationary solution using the CR transport equation (neglecting convection and re-acceleration effects):

$$\frac{\partial}{\partial t} \left(\frac{dn_e}{dE_e} \right) = \nabla \left[D(E_e, \mathbf{x}) \nabla \frac{dn_e}{dE_e} \right] + \frac{\partial}{\partial E_e} \left[b(E_e, \mathbf{x}) \frac{dn_e}{dE_e} \right] + q_e(E_e, \mathbf{x}), \quad (19)$$

where $D(E_e, \mathbf{x})$ denotes the diffusion coefficient and $b(E_e, \mathbf{x})$ the energy loss term. The source function $q_e(E_e, \mathbf{x})$ yields the number of electrons and positrons produced per unit time, energy and volume element at the position \mathbf{x} :

$$q_e(E_e, r) = \sum_f \frac{dN_{e,f}}{dE_e}(E_e) B_f \Gamma_f(r), \quad (20)$$

where the annihilation rate density $\Gamma_f(r)$ is defined in Eq. (6). The sum runs over the kinematically allowed annihilation final states f , each with a branching ratio B_f and a differential spectrum $\frac{dN_{e,f}}{dE_e}$ that represents the number of electrons plus positrons resulting from an annihilation event. For neutralinos annihilating directly into electrons and positrons we model the spectral distribution with $\frac{dN_{e,f}}{dE_e} = 2\delta(E_e - m_\chi c^2)$. We use DarkSUSY to compute both the spectra when neutralinos annihilate directly into a μ^+ and μ^- in the leptophilic model as well as in the four BM models where a fraction of the annihilating neutralinos is converted into electrons and positrons (see Sect. IIB for further details).

The electrons and positrons lose their energy on a timescale that is shorter than the diffusive timescale in the ICM of galaxy clusters for CR electrons with $E_e \gtrsim \text{MeV}$ (CHECK). Hence, we neglect the first term of the r.h.s. in Eq. (19), and derive an expression for the

equilibrium number density:

$$\frac{dn_e}{dE_e}(E_e, r) = \frac{1}{b(E_e, r)} \int_{E_e}^{m_\chi c^2} dE'_e Q(E'_e, r), \quad (21)$$

$$b(E_e, r) = \tilde{b} \left[\frac{B_{\text{CMB}}^2}{8\pi} + \frac{B^2(r)}{8\pi} + u_{\text{SD}}(r) \right] E_e^2, \quad (22)$$

$$\tilde{b} = \frac{4\sigma_{\text{T}}c}{3(m_e c^2)^2}. \quad (23)$$

Here we include the three main radiative loss processes for the CR electrons and positrons: (1) IC losses on CMB photons where the equivalent field strength of the CMB is denoted by $B_{\text{CMB}} = 3.24(1+z)^2 \mu\text{G}$. (2) Synchrotron losses on ambient magnetic fields where we parameterize the magnetic field in the galaxy cluster by $B(r) = 3\mu\text{G} [n_e(r)/n_e(0)]^{\alpha_B}$, which follows from flux frozen magnetic fields. We adopt a magnetic decline of $\alpha_B = 0.7$ in this work. (3) IC losses on starlight and dust with an energy density $u_{\text{SD}}(r)$ given by Eq. (37), which we derive in the following subsection.

IC – dust and starlight

Galaxy clusters are typically characterized by the hot gas in the ICM and the collection of gravitationally bound galaxies. The emission in the IR and UV wavelengths emerge from dust and starlight in both the galaxies and the ICM (e.g. [44] and [45]). Much of the radiation leaks out from the galaxy into the ICM, which give rise to similar spectral distributions for the galaxies and the ICM in these wavelengths. Hence, we use the accurately measured light from galactic dust and starlight for the ISM to model the ICM. We characterize the spectra through a fit to the galactic spectra presented in [44]. The spatial distribution of the SD light in clusters is extracted from a stacked emission analysis of Sloan Digital Sky Survey (SDSS) data at the redshift $z \sim 0.25$ [46]. Finally, we fix the normalization for the light from stars and dust in a galaxy cluster individually using the IR to X-ray luminosity scaling relation found in [47]. The X-ray luminosities for the clusters used in this work are listed in the extended HIGHEST X-ray FLUX Galaxy Cluster Sample (HIFLUGCS) [48] from the Rosat all-sky survey. Note that we have added the Virgo cluster to the sample that we nevertheless refer to as extended HIFLUGCS catalogue in the following.

Spatial distribution – stars and dust

Our goal in this section is to derive a simple spatial model for the distribution of stars and dust in galaxy clusters. For this reason we use stacked cluster observations by Sloan in the r -band that trace the stars. We assume that the dust trace the stars in the clusters, which should be accurate to the order of magnitude estimate that we are interested in here. The stacked surface brightness profiles in [46] are measured at redshift $z \sim 0.25$ with an average mass of the clusters of $4.0 \times 10^{13} M_\odot$. The profiles are build up out of three components; diffuse intracluster light (ICL), galaxies, and the brightest cluster galaxy (BCG) in the center of clusters. However, the total volume overlap of the ISM to the cluster is very small

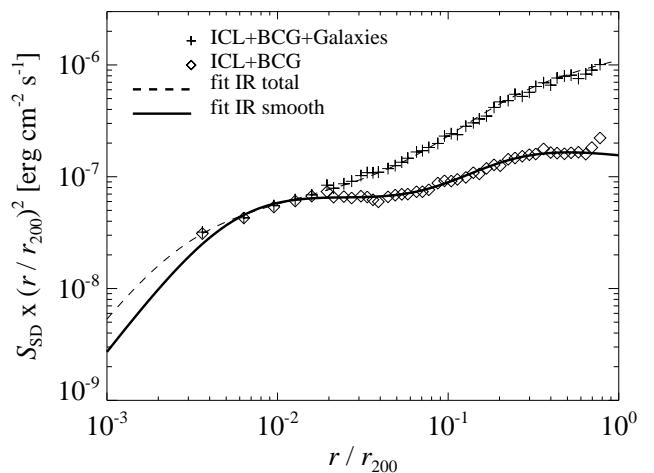


FIG. 3. *Spatial dependence of light from stars and dust.* We show 2D surface brightness profiles in the r -band ($\sim 1\text{eV}$) obtained from stacked clusters in the Sloan Digital Sky Survey (SDSS) at the redshift $z \sim 0.25$ [46]. The brightness profiles have been weighted with the r_{200} normalized area inside radius r , and trace the radial dependence of the luminosity from stars and galaxies. The crosses show the total observed star light including the diffuse intracluster (ICL), the galaxies, and the brightest cluster galaxy (BCG) in the center of the cluster. The diamonds denote the observed star light from the ICL and the BCG. The solid line show the fit to the data of the total light including the ICL, the BCG, and the galaxies, while the smooth component is represented by the dashed line that is fitted to only the ICL and the BCG.

compared to the ICL- and BCG overlap with the cluster, thus the relative contribution of the galaxies to the IC emission is suppressed. To remove this bias we cut out the galaxies that have been smoothed over the cluster in the stacked analysis. In Fig. 3 we show the SDSS stacked brightness profiles as well as the fitted profiles[49]. Our benchmark spatial model are show with the solid black line, and include the contribution from the ICL and BCG.

Instead of modelling the surface brightness with a de Vaucouleur profile with the addition of a power-law, we use a double beta profile model for simplicity of deprojection given by:

$$S_{\text{SD}}(r_\perp) = \sum_{i=1}^2 S_i \left[1 + \left(\frac{r_\perp}{r_{c_i}} \right)^2 \right]^{-3\beta_i+1/2}, \quad (24)$$

where we found the following best fitted central brightness (S_i), core radius (r_{c_i}), and slope (β_i):

$$\begin{aligned} S_1 &= 1.4 \times 10^{-5} \text{ erg cm}^{-2} \text{ s}^{-1}, \quad r_{c_1} = 210 \text{ kpc}, \quad \beta_1 = 0.44 \\ S_2 &= 6.0 \times 10^{-3} \text{ erg cm}^{-2} \text{ s}^{-1}, \quad r_{c_2} = 2.8 \text{ kpc}, \quad \beta_2 = 0.45. \end{aligned} \quad (25)$$

The 3D spatial profile is derived by deprojecting the surface brightness in Eq. (24) (see e.g. [50] for details about

the deprojection):

$$j(r) = \sum_{i=1}^2 \frac{S_i}{2\pi r_{c_i}} \frac{6\beta_i - 1}{(1 + r^2/r_{c_i}^2)^{3\beta_i}} \mathcal{B}\left(\frac{1}{2}, 3\beta_i\right), \quad (26)$$

where $\mathcal{B}(a, b)$ denotes the beta-function [51].

Spectral distribution – stars and dust

Our goal in this section is to derive a simple spectral model for stars and dust in galaxy clusters. Since the radiation from galaxies are expected to leak out into the ICM, we expect similar spectral distributions, at least to the order of magnitude that we are interested in here. Hence, we use the IR to UV spectrum derived in [44] for a MW type galaxy to characterize the spectral distribution of dust and starlight in a cluster. Note, however, that we only keep the spectral shape, and renormalize the spectral distribution using the luminosity from stars and dust.

In Fig. 4 we show the SD spectral distribution together with the CMB black-body distribution in a galaxy cluster, both at the radius $r = 0.071r_{200}$ where the smooth energy density of the SD light (see fig ??) equals the energy density of the CMB. We have renormalized both the spectral SD data and the fitted SD spectra using the luminosity from stars and dust individually (see below for further details about the renormalization). We choose to fit the spectrum of the dust that peaks at about 10^{-2} eV with a double power-law, and the slightly wider spectral distribution of the stars that peaks at about 1 eV with a tiple power-law. We find the best fit spectra for the SD in a cluster through:

$$E_{\text{ph}}^2 \frac{d^2 N_{\text{ph}}}{dE_{\text{ph}} dV} \equiv u_{\text{SD}}(E_{\text{ph}}) = \sum_i N_i(L_X) u_i^{\text{gal}}(E_{\text{ph}}), \quad (27)$$

where $i = \{\text{stars, dust}\}$ and

$$u_{\text{stars}}^{\text{gal}}(E_{\text{ph}}) = \frac{23 \text{ eV}}{\text{cm}^3} \left(\frac{1.23 \text{ eV}}{E_{\text{ph}}} \right)^{1.9} \times \left[1 + \left(\frac{2.04 \text{ eV}}{E_{\text{ph}}} \right)^{20} \right]^{-\frac{1.9}{20}} \times \left[1 + \left(\frac{0.78 \text{ eV}}{E_{\text{ph}}} \right)^{20} \right]^{-\frac{2.6}{20}}, \quad (28)$$

$$u_{\text{dust}}^{\text{gal}}(E_{\text{ph}}) = \frac{40 \text{ eV}}{\text{cm}^3} \left(\frac{0.0144 \text{ eV}}{E_{\text{ph}}} \right)^{4.9} \times \left[1 + \left(\frac{0.0144 \text{ eV}}{E_{\text{ph}}} \right)^{1.9} \right]^{-4.9}. \quad (29)$$

Normalization

HARD TO READ, TO MUCH DETAIL, MOVE TO APPENDIX?, MABEY KEEP NORM CONSTATS AND A VERY SHORT SUMMARY?? The spatial and spectral distribution functions of the light from stars and dust in a cluster are both normalized with a constant determined from the luminosity in each respective wavelength. The

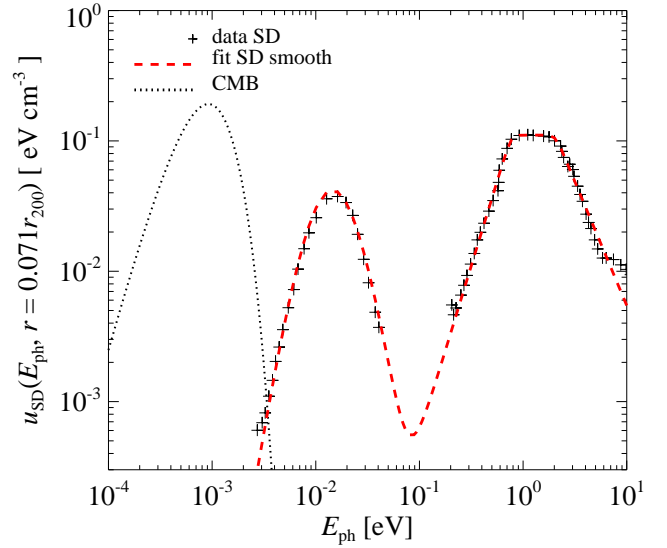


FIG. 4. Spectral dependence of radiation fields in a cluster of galaxies. The black dotted line in the left peak show the spectrum of CMB photons using a black body with a temperature of 2.73 K. The crosses in the middle and right peaks represent the measured spectra from stars and dust (SD), respectively, and are derived in [44] for a galaxy. We normalize the individual SD spectrum separately using the observed luminosity from SD in clusters. The SD luminosity is related to the cluster mass through Eq. where we use have used the mass $M_{200} = 4.0 \cdot 10^{13} M_{\odot}$ in this figure. Finally we renormalize the SD spectra to the radius $r = 0.071r_{200}$, where the smooth energy density of the SD light (see fig ??) equals the energy density of the CMB. The red dashed lines show the fitted SD spectral model.

specific energy density is given by

$$u_{\text{SD}}(E_{\text{ph}}, r) = \frac{j(r)}{j(0)} u_{\text{SD}}(E_{\text{ph}}) = \frac{j(r)}{j(0)} \sum_i N_i(L_X) u_i^{\text{gal}}(E_{\text{ph}}), \quad (30)$$

where we fix the unitless normalization $N_i(L_X)$ using the total energy of the light in stars and dust ($E_{i,\text{vir}}$) within r_{200} :

$$E_{i,\text{vir}} = L_i \frac{r_{200}}{c} = N_i(L_X) \int_{r_{200}} \int_i \frac{j(r)}{j(0)} \frac{u_i^{\text{gal}}(E_{\text{ph}})}{E_{\text{ph}}} dV dE_{\text{ph}}, \quad (31)$$

for $i = \{\text{stars, dust}\}$.

Here we approximate the total energy of the photons within r_{200} with the luminosity L_i [47] times the typical timescale it takes for a photon to propagate through the cluster (we assume that the cluster is optically thin). Once we estimated the SD luminosities for a well representative cluster, we use a IR to X-ray scaling relation to estimate the luminosity from an arbitrary cluster with

mass M_{200} :

$$L = 1.05 \times 10^{45} \text{ erg s}^{-1} \left(\frac{L_X}{10^{44} \text{ erg s}^{-1}} \right)^{0.53}, \quad (32)$$

where L_X is the luminosity of the X-ray emitting gas within r_{200} .

The normalization constant for the star light $[N_{\text{stars}}(L_X)]$ is derived in the following three steps: (1) We use the average apparent magnitude in the $(r+i)$ -band $m_{(r+i),0.25} \approx 15.5$ [46] of a cluster with the average mass $M_{200} = 4.0 \times 10^{13} M_{\odot}$ at a redshift $z = 0.25$ to derive the luminosity from the stars:

$$L_{\text{stars}} = 10^{\frac{m_{\odot} - m_{(r+i),0.25}}{2.5}} \left(\frac{d_{\text{cl}}}{d_{\odot}} \right)^2 L_{\odot} \approx 7.1 \times 10^{44} \text{ erg s}^{-1}, \quad (33)$$

where the apparent magnitude of the sun $m_{\odot} \approx -27.1$, the distance to the sun $d_{\odot} = 4.85 \times 10^{-6} \text{ pc}$, the luminosity of the sun $L_{\odot} = 3.85 \times 10^{34} \text{ erg s}^{-1}$, and the distance to the cluster $d_{\text{cl}} = 1.26 \times 10^9 \text{ pc}$. (2) We use the IR to X-ray scaling relation in Eq. (32) to find a more general form of the luminosity from stars in Eq. (33) that is valid for an arbitrary cluster mass. The cluster X-ray luminosities are found in the extended HIFLUGCS catalogue [48] to which we have added the Virgo cluster. (3) The normalization constant for the stars is determined from the above steps together with Eq. (31) where we integrate over the cluster volume and spectral distribution of the stars. It is given by

$$N_{\text{stars}}(L_X) = 1.2 \times 10^{-9} \left(\frac{L_X}{10^{44} \text{ erg s}^{-1}} \right)^{0.53}. \quad (34)$$

Note that since the luminosities include the contribution from galaxies, we have integrated the spatial distribution including galaxies to derive the normalization. Once the normalization is fixed, the SD energy densities are derived from the spatial distribution where galaxies have been excluded.

The normalization constant for the dust $[N_{\text{dust}}(L_X)]$ is derived in the following four steps: (1) We use a cluster with the average mass $M_{200} = 4.0 \times 10^{13} M_{\odot}$ and estimate the X-ray luminosity from the X-ray to mass scaling relations derived for the Representative XMM-Newton Cluster Structure Survey (REXCESS) in [52]:

$$L_X = 1.18 \times 10^{44} \text{ erg s}^{-1} \left(\frac{M_{200}}{10^{14} M_{\odot}} \right)^{1.81}, \quad (35)$$

where we have used that $M_{200} \approx 1.58 M_{500}$ for a small cluster [53]. (2) From the IR to X-ray scaling relation in Eq. (32) we can now estimate calculate the luminosity from the dust for a $M_{200} = 4.0 \times 10^{13} M_{\odot}$ cluster; $L_{\text{dust}} = 4.7 \times 10^{44} \text{ erg s}^{-1}$. (3) We generalize Eq. (33) to

an arbitrary cluster mass using Eq. (32) together with the cluster X-ray luminosities in the extended HIFLUGCS catalogue. (4) The normalization constant for the dust can now be determined from the above steps together with Eq. (31) where we integrate over the cluster volume and spectral distribution of the dust. It is given by

$$N_{\text{dust}}(L_X) = 1.4 \times 10^{-9} \left(\frac{L_X}{10^{44} \text{ erg s}^{-1}} \right)^{0.53}. \quad (36)$$

Note that since the luminosities include the contribution from galaxies, we have integrated the spatial distribution including galaxies to derive the normalization. Once the normalization is fixed, the SD energy densities are derived from the spatial distribution where galaxies have been excluded.

Energy density

The energy density from starlight and dust in a galaxy cluster is given by

$$\begin{aligned} u_{\text{SD}}(r) &= \int dE_{\text{ph}} \frac{d^2 N_{\text{ph}}}{dE_{\text{ph}} dV} E_{\text{ph}} = \int dE_{\text{ph}} \frac{u_{\text{SD}}(E_{\text{ph}}, r)}{E_{\text{ph}}} \\ &= \frac{j(r)}{j(0)} \int dE_{\text{ph}} \sum_i N_i(L_X) u_i^{\text{gal}}(E_{\text{ph}}). \end{aligned} \quad (37)$$

In Fig. 5 we compare the energy densities from different radiation fields in a galaxy cluster with the mass $M_{200} = 4.0 \times 10^{13} M_{\odot}$. We use two different profiles for the SD energy density, where the total includes the ICL, the BCG and all the galaxies, while the galaxies are excluded in the smooth contribution. We find that even for a cluster with a relative small mass the energy density of the SD components dominates over the CMB and the magnetic fields (with a central B field of $3 \mu\text{G}$) within about 10% of r_{200} . Outside this radius the CMB is dominating the energy density of the cluster, hence the density of the magnetic fields are always subdominant in the cluster and can safely be removed from cluster IC calculations for reasonable central densities and spectral index. Although, in this work we keep its contribution to the total energy density for consistency.

(DELETED TEXT)

III. SPECTRAL GAMMA-RAY DISTRIBUTION

IV. SURFACE BRIGHTNESS PROFILES

V. POPULATION STUDIES

Model predictions

We wish to thank...

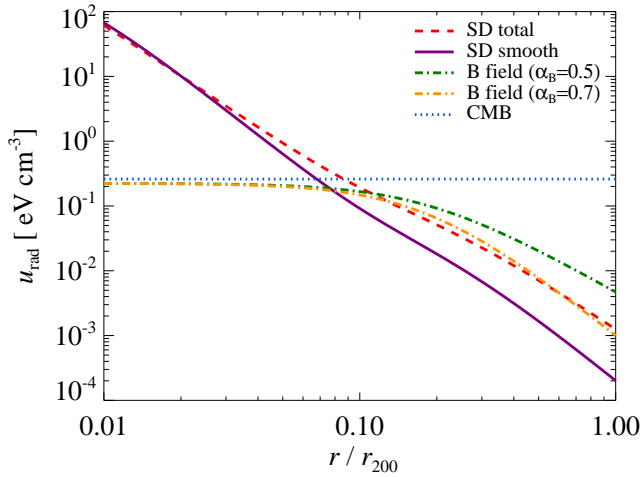


FIG. 5. Spatial dependence of the energy density of radiation fields in a cluster of galaxies. The energy density of the CMB, shown by the blue dotted line, is isotropic throughout the cluster, hence represented by a flat profile with $u_{\text{cmb}} = 0.26 \text{ eV cm}^{-3}$. The energy density of the light from stars and dust (SD) is denoted by the red dashed line and the solid purple line for the total SD light and the smooth SD light, respectively. The SD light has been renormalized to a cluster with the mass $M_{200} = 4.0 \cdot 10^{13} M_{\odot}$. Finally we show the energy density two magnetic field models with a central magnetic field of $3 \mu\text{G}$. The magnetic field scales with the gas density to the power α_B ; green dash-dotted line ($\alpha_B = 0.5$) and orange dash-dotted line ($\alpha_B = 0.7$). Note that the SD radiation is dominating the energy density inside $\sim 0.1 r_{200}$.

-
- [1] M. Pato, L. Baudis, G. Bertone, R. R. de Austri, L. E. Strigari, *et al.*, (2010), * Temporary entry *, arXiv:1012.3458 [astro-ph.CO].
- [2] J. R. Ellis, J. L. Feng, A. Ferstl, K. T. Matchev, and K. A. Olive, *Eur.Phys.J.* **C24**, 311 (2002), arXiv:astro-ph/0110225 [astro-ph].
- [3] H. Baer, A. Mustafayev, S. Profumo, and X. Tata, *Phys.Rev.* **D75**, 035004 (2007), arXiv:hep-ph/0610154 [hep-ph].
- [4] V. Khachatryan *et al.* (CMS Collaboration), (2011), * Temporary entry *, arXiv:1101.1628 [hep-ex].
- [5] L. Bergstrom, *New J.Phys.* **11**, 105006 (2009), arXiv:0903.4849 [hep-ph].
- [6] CTA, (2010), The CTA Consortium: Design Concepts for the Cherenkov Telescope Array, arXiv:1008.3703 [astro-ph.IM].
- [7] L. Bergstrom, T. Bringmann, and J. Edsjo, (2010), * Temporary entry *, arXiv:1011.4514 [hep-ph].
- [8] D. Hooper and L. Goodenough, *ArXiv e-prints* (2010), arXiv:1010.2752 [hep-ph].
- [9] A. Boyarsky, D. Malyshev, and O. Ruchayskiy, *ArXiv e-prints* (2010), arXiv:1012.5839 [hep-ph].
- [10] T. Bringmann, M. Doro, and M. Fornasa, *JCAP* **1**, 16 (2009), arXiv:0809.2269.
- [11] V. A. Acciari, T. Arlen, T. Aune, M. Beilicke, W. Benbow, D. Boltuch, S. M. Bradbury, J. H. Buckley, V. Bugaev, K. Byrum, A. Cannon, A. Cesarini, J. L. Christiansen, L. Ciupik, W. Cui, R. Dickherber, C. Duke, J. P. Finley, G. Finnegan, A. Furniss, N. Galante, S. Godambe, J. Grube, R. Guenette, G. Gyuk, D. Hanna, J. Holder, C. M. Hui, T. B. Humensky, A. Imran, P. Kaaret, N. Karlsson, M. Kertzman, D. Kieda, A. Konopelko, H. Krawczynski, F. Krennrich, G. Maier, S. McArthur, A. McCann, M. McCutcheon, P. Moriarty, R. A. Ong, A. N. Otte, D. Pandel, J. S. Perkins, M. Pohl, J. Quinn, K. Ragan, L. C. Reyes, P. T. Reynolds, E. Roache, H. J. Rose, M. Schroedter, G. H. Sembroski, G. D. Senturk, A. W. Smith, D. Steele, S. P. Swordy, G. Tešić, M. Theiling, S. Thibadeau, A. Varlotta, V. V. Vassiliev, S. Vincent, R. G. Wagner, S. P. Wakely, J. E. Ward, T. C. Weekes, A. Weinstein, T. Weisgarber, D. A. Williams, S. Wissel, B. Zitzer, and VERITAS Collaboration, *Astrophys. J.* **720**, 1174 (2010), arXiv:1006.5955 [astro-ph.CO].
- [12] P. Scott, J. Conrad, J. Edsjö, L. Bergström, C. Farnier, and Y. Akrami, *JCAP* **1**, 31 (2010), arXiv:0909.3300 [astro-ph.CO].
- [13] M.-L. Garde, Talk at IDM10, Montpellier, France, July 2010, to appear in the Proceedings.
- [14] A. Pinzke, C. Pfrommer, and L. Bergström, *Physical Review Letters* **103**, 181302 (2009), arXiv:0905.1948 [astro-ph.HE].

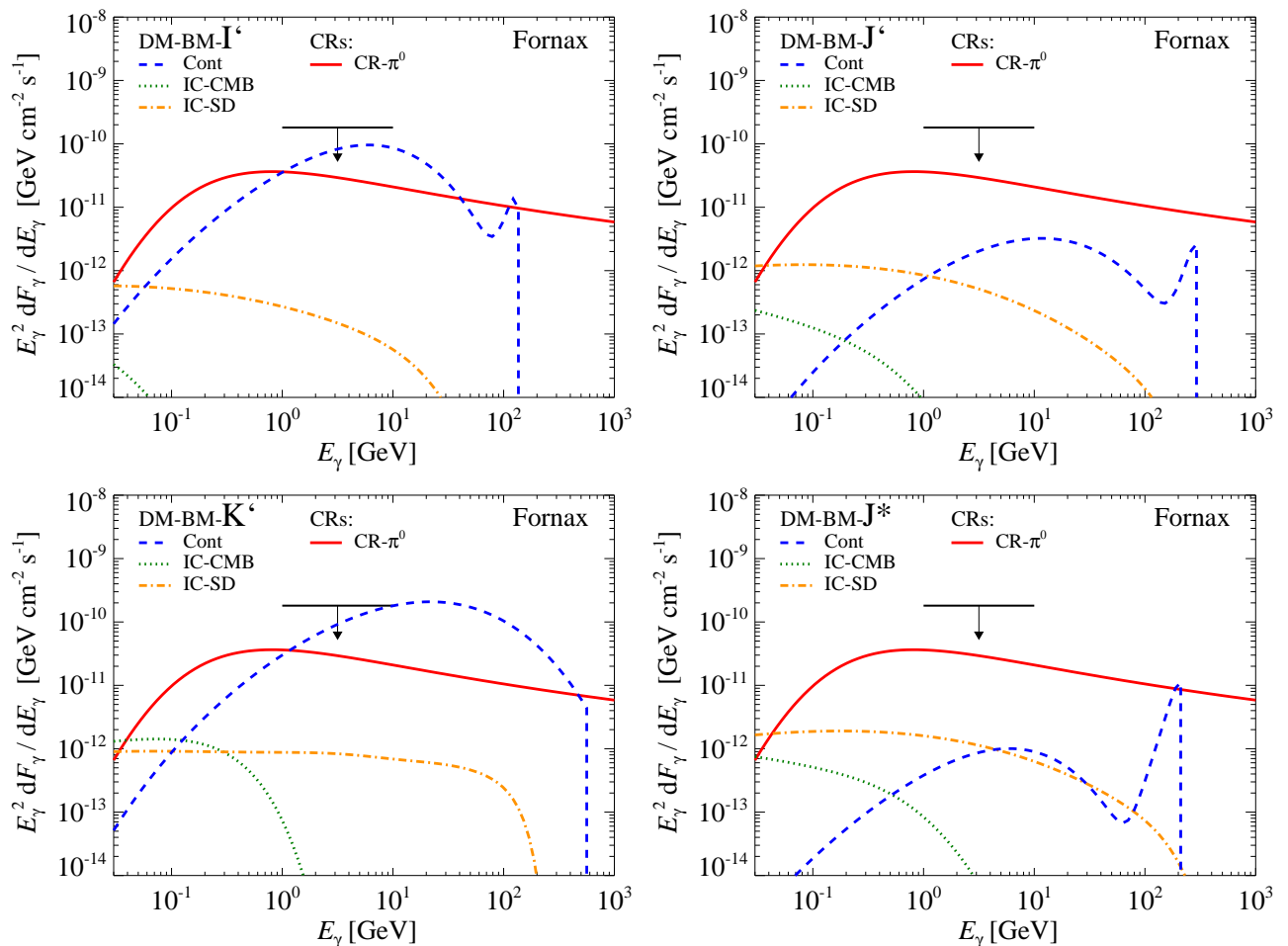


FIG. 6. Comparing the differential flux from different models: we show the continuum emission from DM benchmark (BM) models (blue), electrons and positrons from DM BM models that inverse Compton upscattered both CMB photons (orange) as well as dust and star photons (green), and CR induced gamma-ray emission (red solid). The various linestyles are associated with individual DM BM models; I* (dotted), K* (dashed), and J* (dash-dotted). The emission is calculated for the Fornax cluster using a point spread function of 0.1 deg and a boost from substructures of ... We find bright prospects for detecting the continuum emission that is dominating the total emission in the GeV energy range. Also note that, above 100 MeV the total inverse Compton emission is at least a factor 10 smaller than the emission expected from both the continuum emission and the emission coming from CRs.

- [15] L. Gao, C. S. Frenk, M. Boylan-Kolchin, A. Jenkins, V. Springel, and S. D. M. White, *MNRAS* **410**, 2309 (2011), arXiv:1006.2882 [astro-ph.CO].
- [16] All halo masses and length scales in this paper are scaled to the currently favored value of Hubble's constant, $H_0 = 70 \text{ km s}^{-1} \text{ Mpc}^{-1}$. We define the virial mass M_{200} and virial radius r_{200} as the mass and radius of a sphere enclosing a mean density that is 200 times the critical density of the Universe ρ_{cr} .
- [17] L. Gao, S. D. M. White, A. Jenkins, F. Stoehr, and V. Springel, *MNRAS* **355**, 819 (2004), arXiv:astro-ph/0404589.
- [18] S. Colafrancesco, S. Profumo, and P. Ullio, *A&A* **455**, 21 (2006), arXiv:astro-ph/0507575.
- [19] T. E. Jeltema, J. Kehayias, and S. Profumo, *Phys. Rev. D* **80**, 023005 (2009), arXiv:0812.0597.
- [20] A. Pinzke and C. Pfrommer, *MNRAS* **409**, 449 (2010), arXiv:1001.5023 [astro-ph.CO].
- [21] A. V. Macciò, A. A. Dutton, and F. C. van den Bosch, *MNRAS* **391**, 1940 (2008), arXiv:0805.1926.
- [22] D. H. Zhao, Y. P. Jing, H. J. Mo, and G. Börner, *Astrophys. J.* **707**, 354 (2009), arXiv:0811.0828.
- [23] W. Hu and A. V. Kravtsov, *Astrophys. J.* **584**, 702 (2003), arXiv:astro-ph/0203169.
- [24] J. F. Navarro, A. Ludlow, V. Springel, J. Wang, M. Vogelsberger, S. D. M. White, A. Jenkins, C. S. Frenk, and A. Helmi, *MNRAS* **402**, 21 (2010), arXiv:0810.1522.
- [25] V. Springel, J. Wang, M. Vogelsberger, A. Ludlow, A. Jenkins, A. Helmi, J. F. Navarro, C. S. Frenk, and S. D. M. White, *MNRAS* **391**, 1685 (2008), arXiv:0809.0898.
- [26] M. Kuhlen, J. Diemand, P. Madau, and M. Zemp, *Journal of Physics Conference Series* **125**, 012008 (2008), arXiv:0810.3614.
- [27] V. Springel, S. D. M. White, C. S. Frenk, J. F. Navarro, A. Jenkins, M. Vogelsberger, J. Wang, A. Lud-

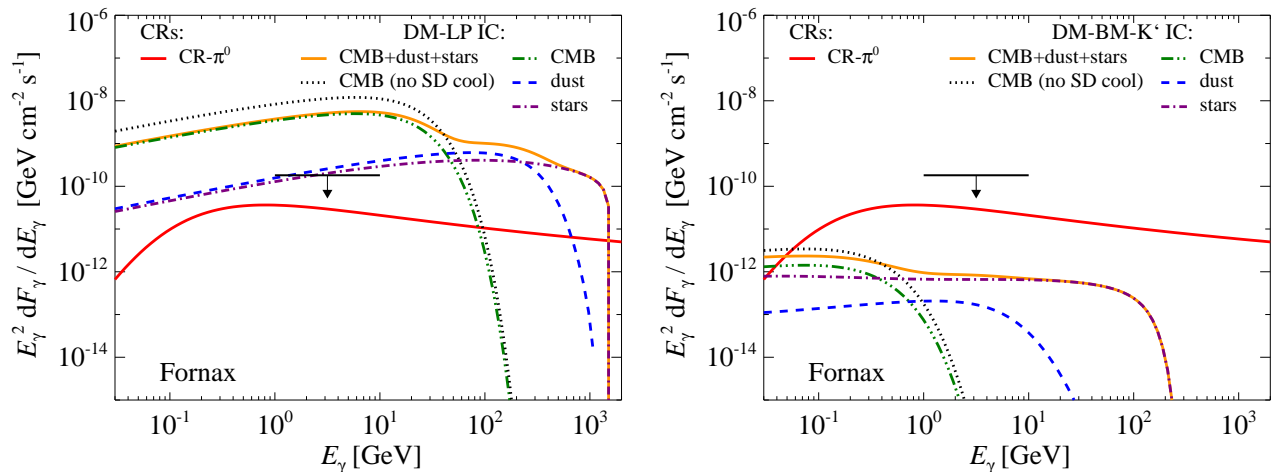


FIG. 7. Comparing the differential flux from different inverse Compton upscattered radiation fields in the Fornax cluster. We show the inverse Compton emission induced by leptophilic DM in the left panel and by the K' benchmark model in the right panel. The contribution from each individual radiation field from top line to bottom line; CMB (green dashed-double-dotted), dust (blue dashed), stars (purple dashed-dotted). The sum of the three components are shown with the orange solid line. The black dotted line represents the upscattered CMB photons without any cooling from stars and dust. The red solid line show the CR induced gamma-ray flux. The black arrow show the differential upper limit from Fermi ADD REF. All fluxes are calculated within r_{200} with a point spread function of 0.1 deg. The boost from Sommerfeld is ..., and from substructures is .

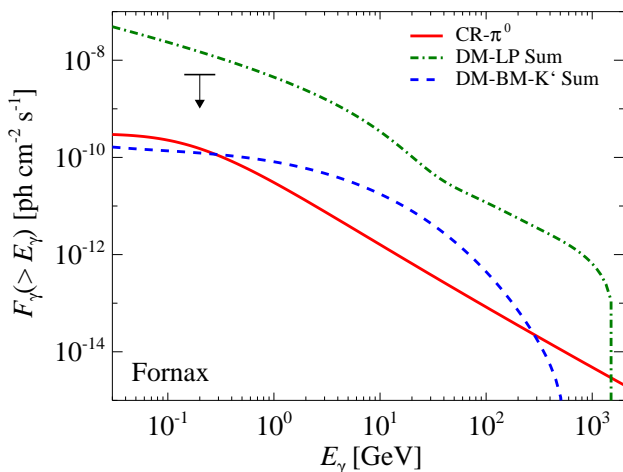


FIG. 8. Comparing the energy integrated flux from different models: we show the emission from leptophilic (LP) models with green lines, K' benchmark model (BM) with blue lines, and the CR induced emission with a red line. The dotted and dashed lines show the inverse Compton (IC) upscattered CMB photons and star and dust photons, respectively. The green solid line show the final state radiation from the LP model, and the solid blue line show the continuum emission from the DM. The black arrow show the integrated flux upper limit set by Fermi. The emission is calculated for the Fornax cluster using a point spread function of 0.1 deg and a boost from substructures of ... We find that LP models are dominating the total flux in the entire energy range, where the IC upscattered CMB photons overproduce the upper limit by a factor 3.

- low, and A. Helmi, *Nature (London)* **456**, 73 (2008), arXiv:0809.0894.
- [28] Our approach of fitting the scaling behavior of $L_{\text{sub}}(< r)$ directly from numerical simulations self-consistently accounts for the radial dependence of the substructure concentration [25].
- [29] S. Hofmann, D. J. Schwarz, and H. Stöcker, *Phys. Rev. D* **64**, 083507 (2001), arXiv:astro-ph/0104173.
- [30] A. M. Green, S. Hofmann, and D. J. Schwarz, *JCAP* **8**, 3 (2005), arXiv:astro-ph/0503387.
- [31] A. B. Newman, T. Treu, R. S. Ellis, and D. J. Sand, *ApJL* **728**, L39+ (2011), arXiv:1101.3553 [astro-ph.CO].
- [32] J. C. Kempner, E. L. Blanton, T. E. Clarke, T. A. Enßlin, M. Johnston-Hollitt, and L. Rudnick, in *The Riddle of Cooling Flows in Galaxies and Clusters of galaxies*, edited by T. Reiprich, J. Kempner, & N. Soker (2004) pp. 335–+, arXiv:astro-ph/0310263.
- [33] L. Feretti, in *Astronomical Society of the Pacific Conference Series*, Astronomical Society of the Pacific Conference Series, Vol. 301, edited by S. Bowyer and C.-Y. Hwang (2003) pp. 143–+.
- [34] C. Ferrari, F. Govoni, S. Schindler, A. M. Bykov, and Y. Rephaeli, *Space Science Reviews* **134**, 93 (2008), arXiv:0801.0985.
- [35] V. S. Berezinsky, P. Blasi, and V. S. Ptuskin, *Astrophys. J.* **487**, 529 (1997).
- [36] M. Jubelgas, V. Springel, T. Enßlin, and C. Pfrommer, *A&A* **481**, 33 (2008), arXiv:astro-ph/0603485.
- [37] T. A. Enßlin, C. Pfrommer, V. Springel, and M. Jubelgas, *A&A* **473**, 41 (2007), arXiv:astro-ph/0603484.
- [38] C. Pfrommer, V. Springel, T. A. Enßlin, and M. Jubelgas, *MNRAS* **367**, 113 (2006), arXiv:astro-ph/0603483.
- [39] E. A. Helder, J. Vink, C. G. Bassa, A. Bamba, J. A. M. Bleeker, S. Funk, P. Ghavamian, K. J. van der Heyden, F. Verbunt, and R. Yamazaki, *Science* **325**, 719 (2009),

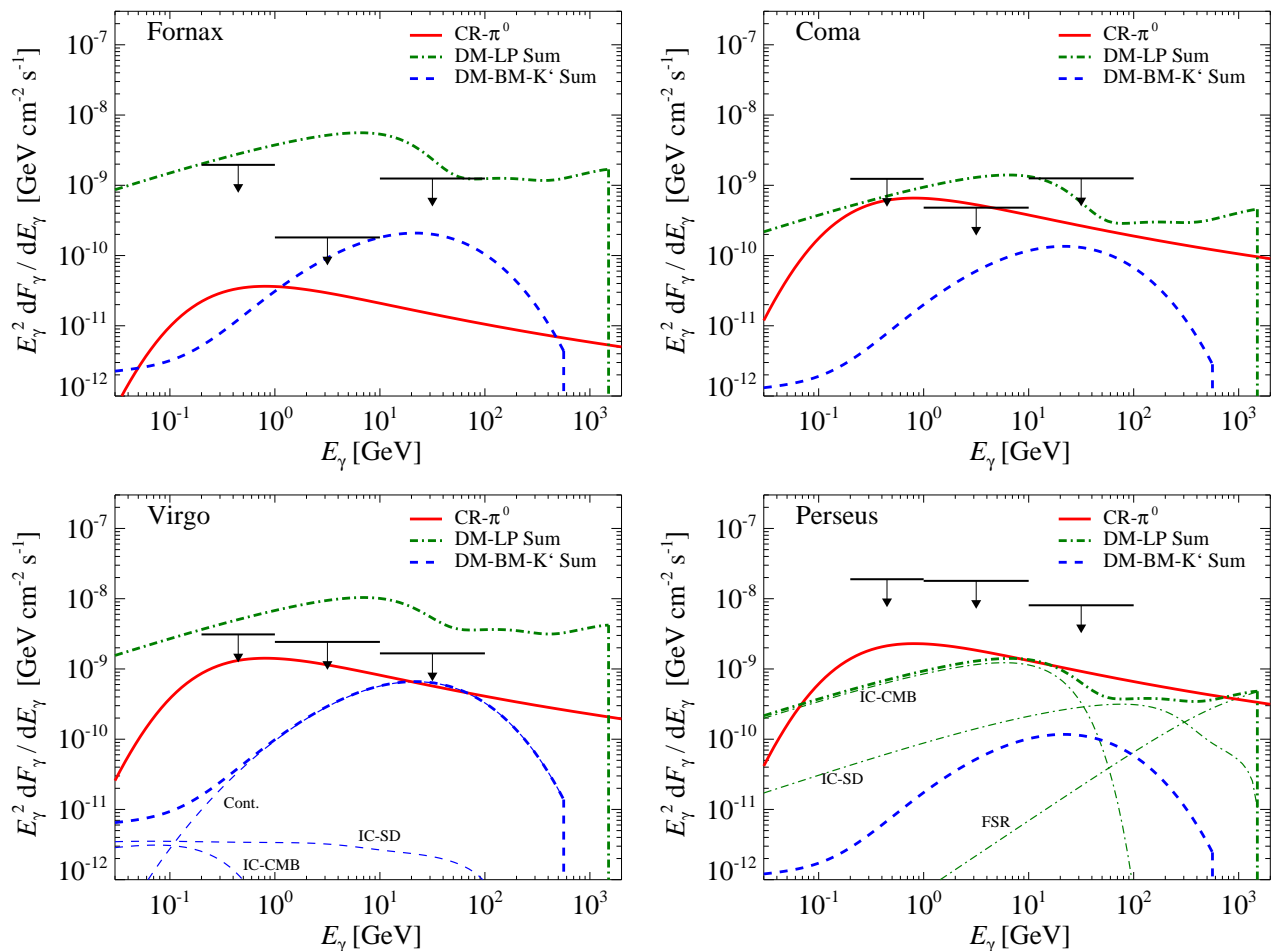


FIG. 9. Comparing the emission from different clusters. The emission from the clusters is calculated using a point spread function of 0.1 deg and includes the boost from substructures. We show the differential flux from four clusters; Fornax (upper left), Coma (upper right), Virgo (lower left), and Perseus (lower right). The different linestyles show; CR induced emission (solid), leptophilic models (LP) include both final state radiation and IC upscattered CMB, dust and star light (dotted), and benchmark K' models (BM) include continuum emission, and IC upscattered CMB, dust and star light (dashed). The arrows have colors matching each cluster and show the differential upper limits set by Fermi in the energy ranges 0.2 – 1 GeV, 1 – 10 GeV, and 10 – 100 GeV from left to right. For visualization we offset the arrows by increasing the mean energy by 30 percent in the opposite order as they appear in the figure, i.e. starting with Perseus. All fluxes are calculated within r_{200} . We find that the lower GeV energy regime is most constraining, and induce upper limits on boost factors.

arXiv:0906.4553 [astro-ph.GA].

- [40] H. Kang and T. W. Jones, *Astrophys. J.* **620**, 44 (2005).
- [41] T. Bringmann, L. Bergström, and J. Edsjö, *Journal of High Energy Physics* **1**, 49 (2008), arXiv:0710.3169 [hep-ph].
- [42] G. B. Rybicki and A. P. Lightman, *Radiative processes in astrophysics* (New York, Wiley-Interscience, 1979., 1979).
- [43] G. R. Blumenthal and R. J. Gould, *Reviews of Modern Physics* **42**, 237 (1970).
- [44] T. A. Porter, I. V. Moskalenko, and A. W. Strong, *ApJL* **648**, L29 (2006), arXiv:astro-ph/0607344.
- [45] R. C. Gilmore, P. Madau, J. R. Primack, R. S. Somerville, and F. Haardt, *MNRAS* **399**, 1694 (2009), arXiv:0905.1144 [astro-ph.CO].
- [46] S. Zibetti, S. D. M. White, D. P. Schneider, and J. Brinkmann, *MNRAS* **358**, 949 (2005), arXiv:astro-ph/0501194.
- [47] M. Giard, L. Montier, E. Pointecouteau, and E. Simmat, *A&A* **490**, 547 (2008), arXiv:0808.2404.
- [48] T. H. Reiprich and H. Böhringer, *Astrophys. J.* **567**, 716 (2002), arXiv:astro-ph/0111285.
- [49] The measured brightness is converted into units of erg s^{-1} using $[?] S(\text{mag}''^{-2}) = \mathcal{M}_{\odot} + 21.572 - 2.5 \log_{10} S(L_{\odot} \text{ pc}^{-2})$, where the sun's absolute magnitude in the r -band is given by $\mathcal{M}_{\odot} = 27.1 [?]$ and the luminosity of the sun by $L_{\odot} = 3.85 \cdot 10^{33} \text{ erg s}^{-1}$.
- [50] C. Pfrommer and T. A. Enßlin, *A&A* **413**, 17 (2004).
- [51] M. Abramowitz and I. A. Stegun, *Handbook of mathematical functions* (Dover, New York, 1965).
- [52] G. W. Pratt, J. H. Croston, M. Arnaud, and H. Böhringer, *A&A* **498**, 361 (2009), arXiv:0809.3784.
- [53] We derive the factor 1.58 using M_{200}/M_{500} for the clusters in the HIFLUGCS catalogue with a mass similar to

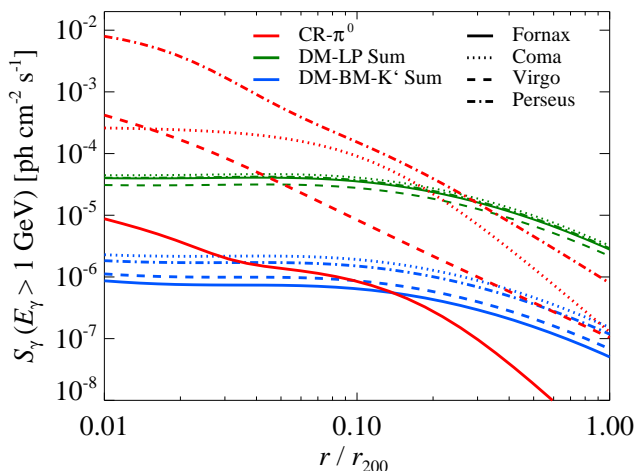


FIG. 10. Comparing the surface brightness from different clusters. We show the surface brightness above the energy 1 GeV. The boost from substructures is included and we use a point spread function of 0.1 deg.

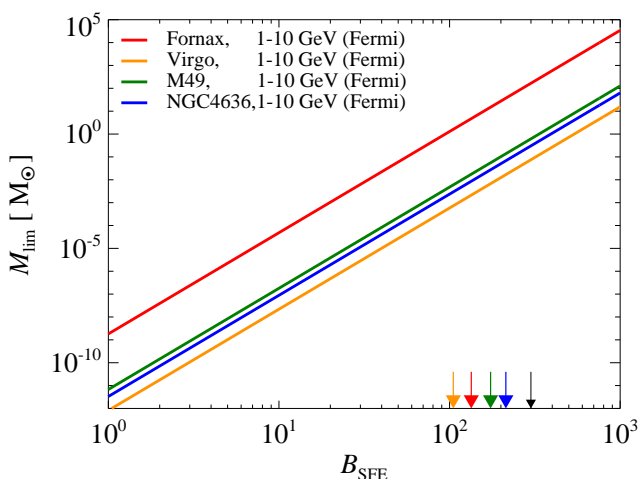


FIG. 11. Constraining leptophilic boost factors using flux upper limits. The emission is derived within r_{200} using a point spread function of 0.1 deg. In order not to overproduce the Fermi differential flux upper limits in the energy interval 1 – 10 GeV the boost from substructures and Sommerfeld enhancement (SFE) is constrained for four clusters; Fornax (red), Virgo (orange), M49 (green), and NGC4636 (Blue). The arrows have colors matching each cluster and indicate the SFE in each cluster. The SFE has been rescaled from 300 that is required to explain the electron and positron excess observed in the Milky Way (MW) with leptophilic dark matter (refer to equation). If the DM interpretation is correct, we can constrain the smallest size of halos to be larger than $10 M_\odot$. However, if the smallest size of DM halos is $10^{-6} M_\odot$, we can constrain the SFE to about 4 in Fornax, corresponding to a maximum SFE in the MW of about 10.

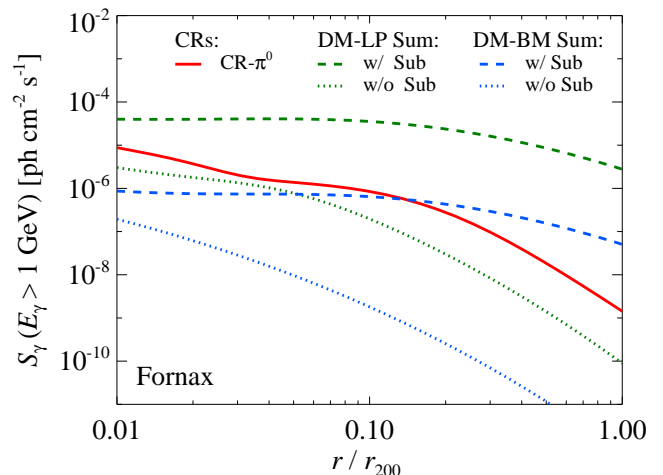


FIG. 12. The impact of substructures on surface brightness. We show the surface brightness at 1 GeV for the Fornax cluster using a very small point spread function of 10^{-5} deg that reveals the details of the spatial profiles. The emission induced by CRs is denoted by the red solid line, the leptophilic models by green lines, and the DM K' benchmark model by blue lines. The dashed and dotted lines include and exclude substructures, respectively. Notice the nearly flat profiles when substructures are included, and the relative large boost at a percent of r_{200} .

$M_{200} = 4.0 \times 10^{13} M_\odot$ that we use to derive the luminosity from dust.

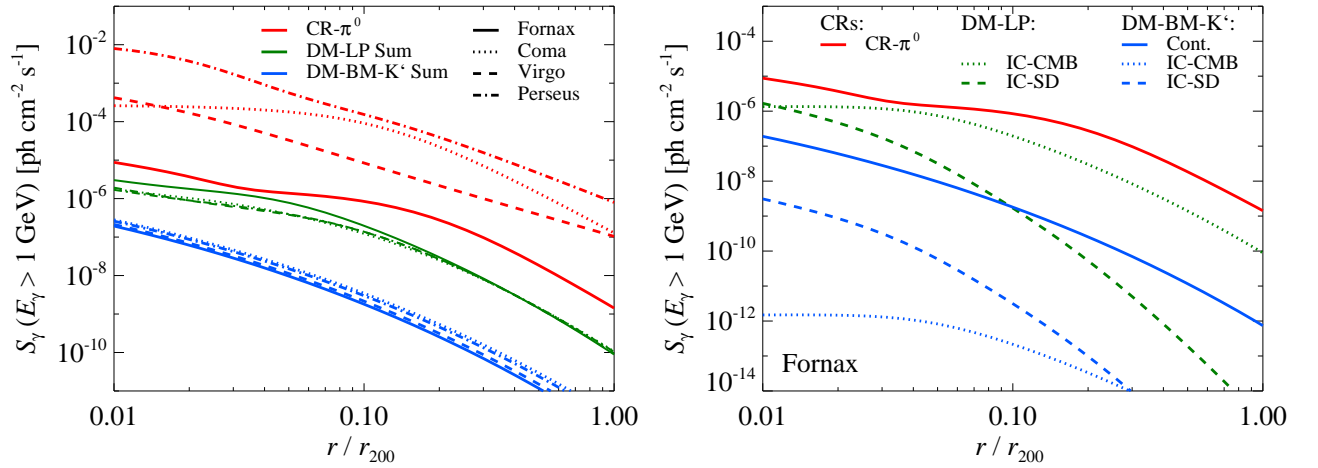


FIG. 13. The surface brightness without substructures. We show the CR induced emission (red), leptophilic emission (green), and emission from the K' benchmark model (blue). The surface brightness above 1 GeV is derived using a very small point spread function ($\theta_{\text{psf}} = 10^{-5}$ deg). LEFT PANEL: compare the surface brightness for different clusters; Fornax (solid), Coma (dotted), Virgo (dashed), and Perseus (dash-dotted). RIGHT PANEL: compare different emission components in Fornax; dotted lines show the inverse Compton (IC) upscattered CMB photons, dashed lines show the IC upscattered photons from stars and dust, and blue solid line show the continuum emission from the K' benchmark model. **(DELETED TEXT)**

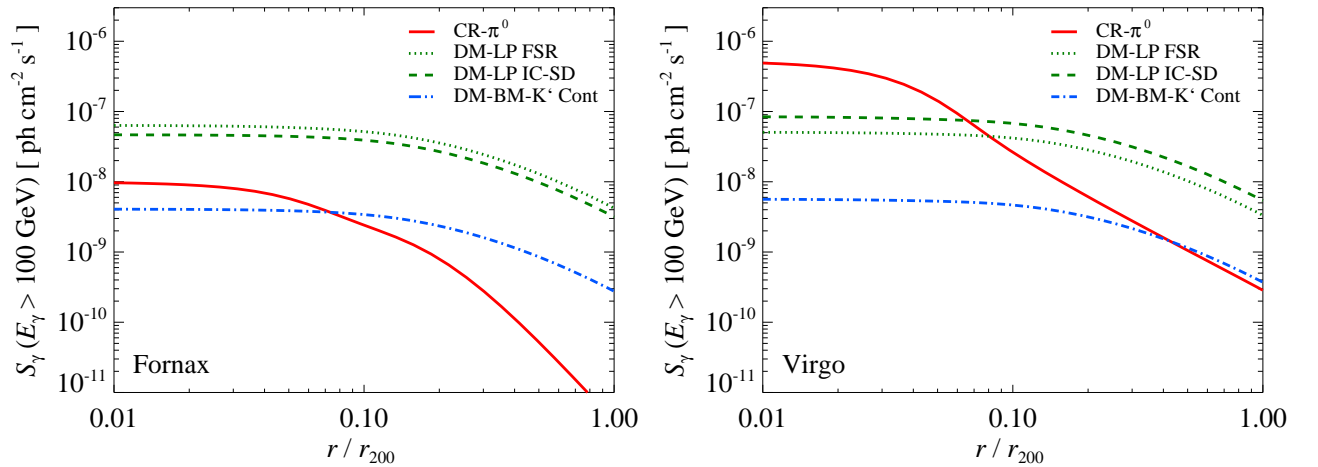


FIG. 14. Surface brightness predicted for Cherenkov telescopes. We show the emission above $E_\gamma = 100$ GeV, include the boost from substructures and use a point spread function of 0.1 deg. Left panel show the Fornax cluster and right panel the Virgo cluster. The emission is derived for the following components; CRs (red solid), continuum emission from the DM K' benchmark model (blue dash-dotted), as well as final state radiation (green dashed) and inverse Compton upscattered dust and star light (green dotted) from leptophilic DM. **(DELETED TEXT)**

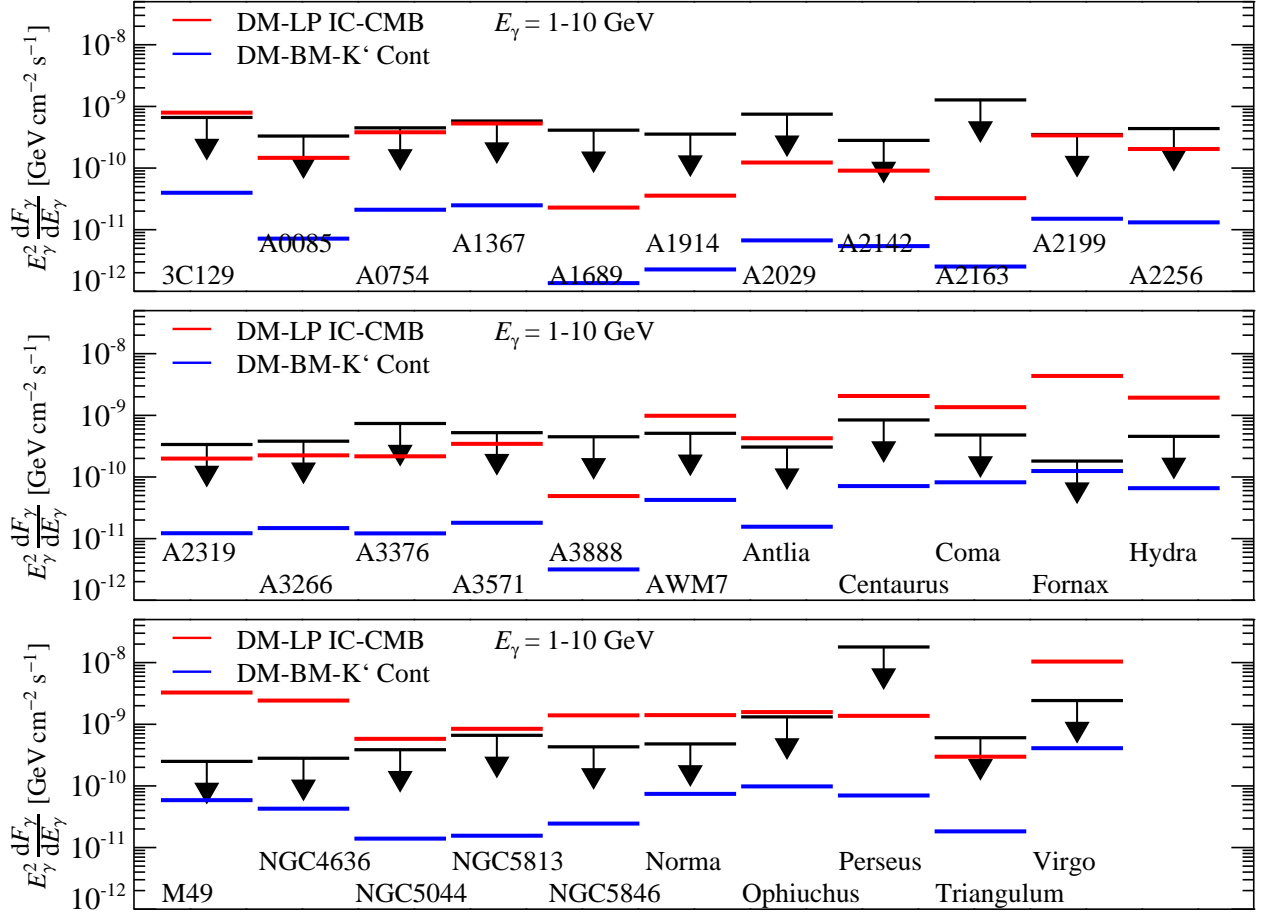


FIG. 15. *Fermi flux upper limits contrasted to the predicted DM gamma-ray flux. We show the mean differential flux in the energy range $E_\gamma = 1 - 10$ GeV for 32 clusters. The Fermi upper limits are shown with black arrows. The predicted fluxes are derived from both a leptophilic DM model that result in inverse Compton upscattered CMB photons (red), and the continuum emission from the DM K' benchmark model (blue). The leptophilic fluxes are ruled out by 14 of the clusters, with the strongest constraints set by Fornax and M49. We can not constrain the benchmark models, although our predictions are approaching the upper limits.*

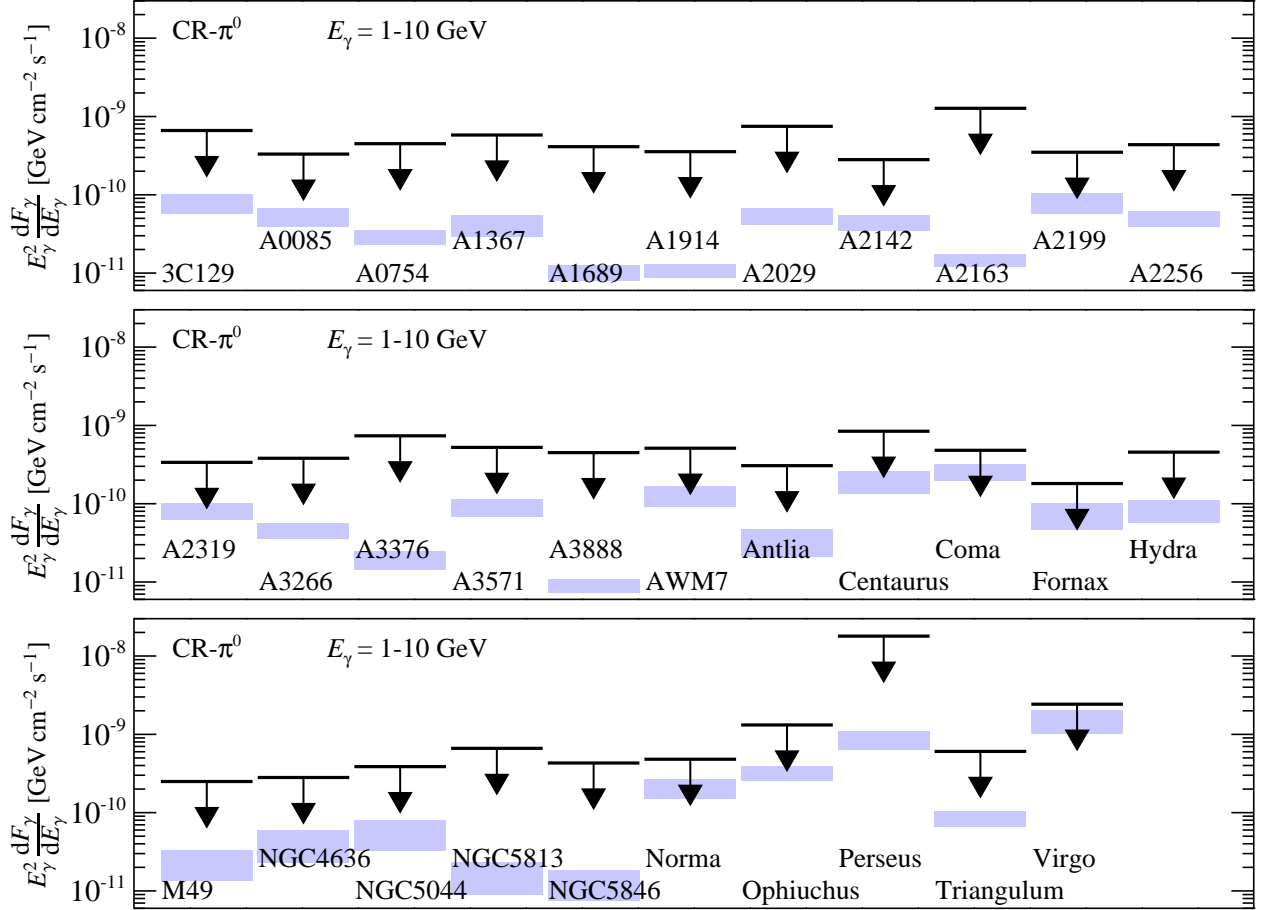


FIG. 16. Fermi flux upper limits contrasted to the predictions by the semi-analytic Pinzke and Pfrommer model for CR induced gamma-ray emission. We show the mean differential flux in the energy range $E_\gamma = 1 - 10 \text{ GeV}$ for 32 clusters. The Fermi upper limits are shown with black arrows. The blue boxes show the gamma-ray emission from CR induced π^0 s decaying, where the upper bound shows the estimates for an optimistic model and the lower bound a more conservative model excluding point sources (the realistic case is more likely in between, see [20] for details). Note that there is currently no tension between our predictions and upper limits from Fermi, although Virgo, Norma, and Coma are close and will in the coming years enforce constraints on the hadronic models.

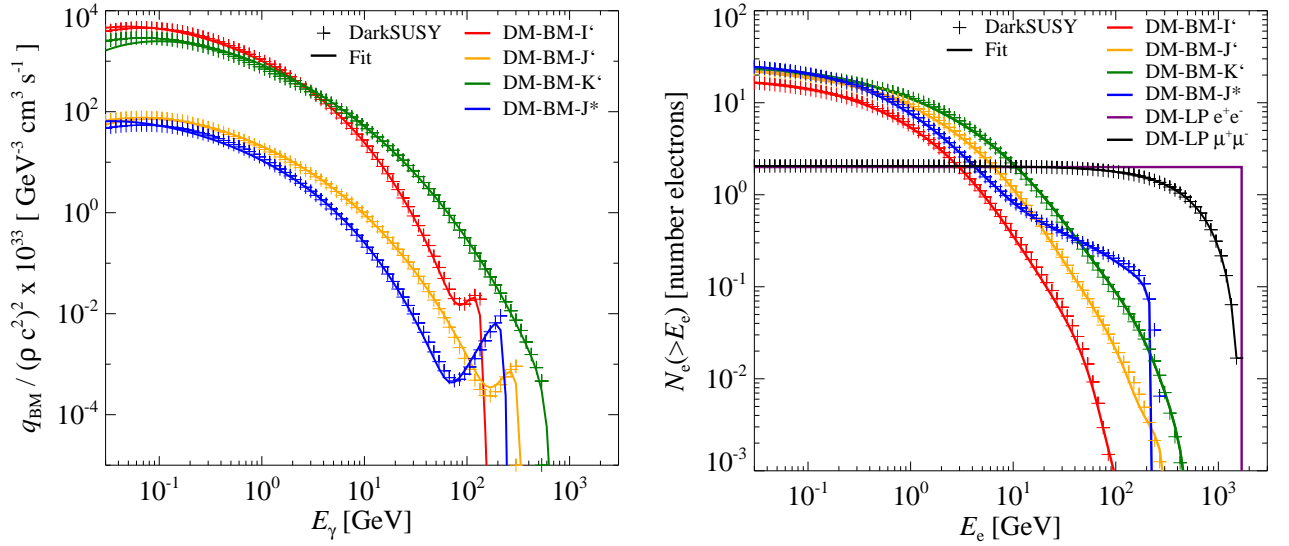


FIG. 17. The underlying source functions for different DM models. Crosses show the simulated data from DarkSUSY and the solid lines show the fit to the data using Eq.... LEFT PANEL: normalized differential continuum spectra for four different DM benchmark (BM) models; I' model (red), J' (orange), K' (green), and J^* (blue). RIGHT PANEL: number of electron and positron per DM annihilation above the electron energy E_e for different dark matter models; I' BM model (red), J' BM model (orange), K' BM model (green), and J^* BM model (blue), leptophilic (LP) DM annihilating into electrons and positrons (purple), and LP DM annihilating into muons (black).

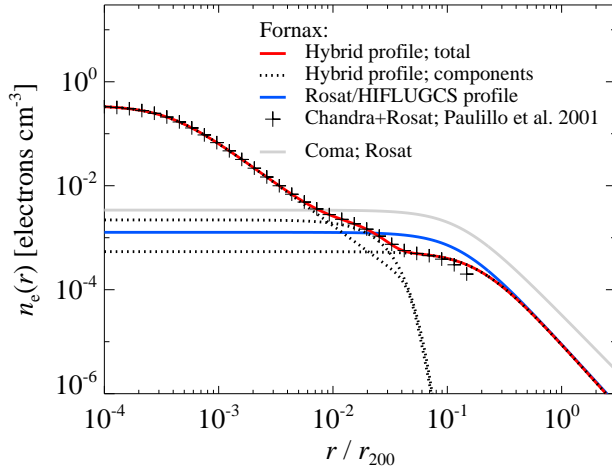


FIG. 18. Comparing different electron number density profiles for the Fornax cluster. Black crosses show the density profile inferred from deprojected Chandra and Rosat X-ray surface brightness observations CITE. The total hybrid profile shown by the red solid line represent the best fit to the data, where the fitted individual density components are shown by the black dotted lines. The blue solid line show the single beta density profile inferred from the HIFLUGCS catalogue. Due to insufficient sensitivity to the outer part in the plotted data, we infer the outer slope found in the HIFLUGCS catalogue.

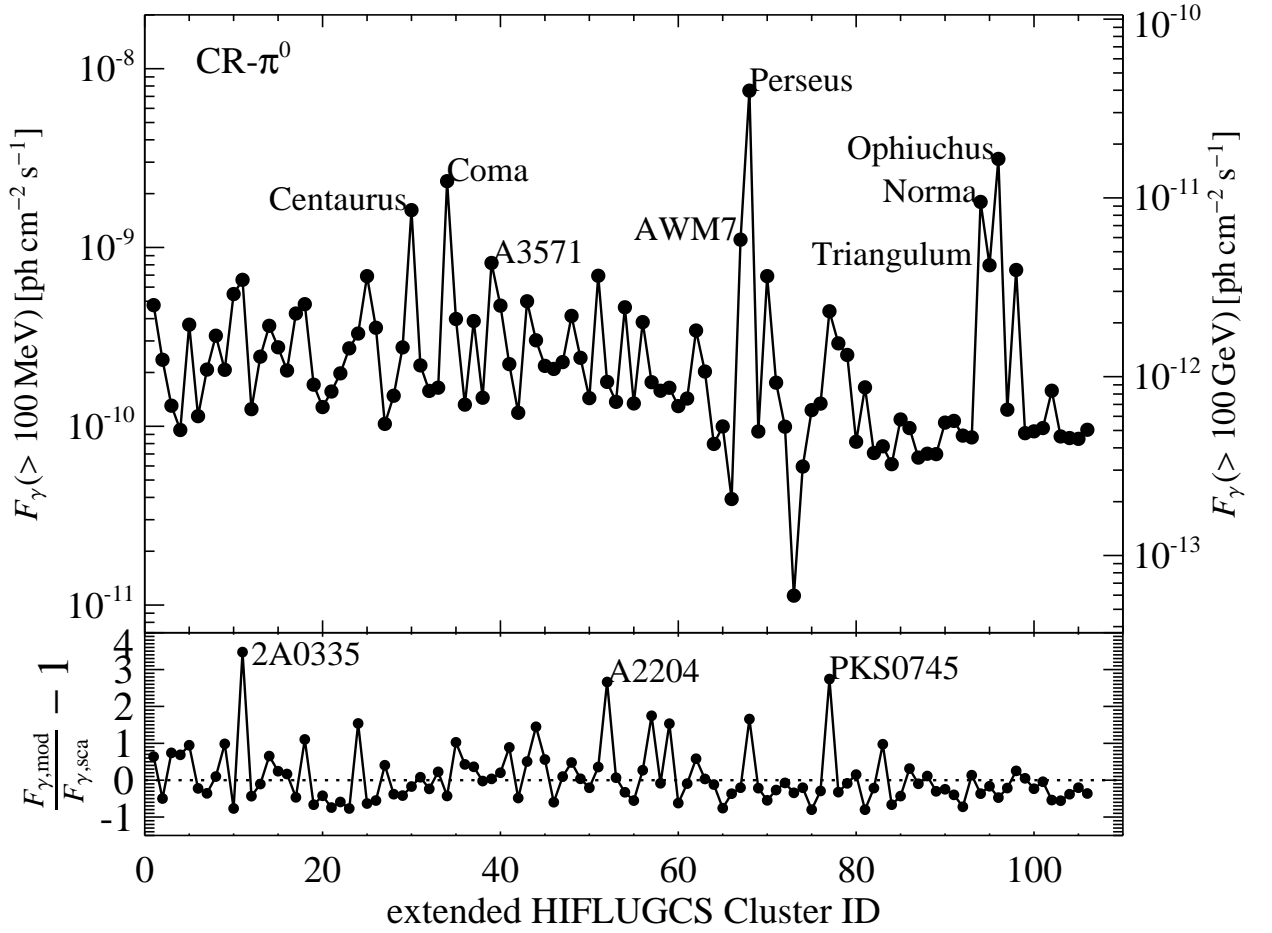


FIG. 19. Comparing the flux from clusters in the extended HIFLUGCS catalogue. We show the energy integrated gamma-ray flux induced by CRs for the 106 clusters included in the extended HIFLUGCS catalogue. The fluxes are calculated within r_{200} , and are derived using a single beta profile for each cluster's gas density profile (see text for details). The upper panel show the energy integrated flux above 100 MeV (left side) and above 100 GeV (right side), both as a function of HIFLUGCS cluster ID. The name of the eight brightest clusters are written out. The lower panel show the relative difference between the gamma-ray flux predicted by mass-luminosity scaling relations compared to the flux computed using the semi-analytically model CITE. The name of the clusters with the largest offset are printed out, which correlate with cool core clusters.

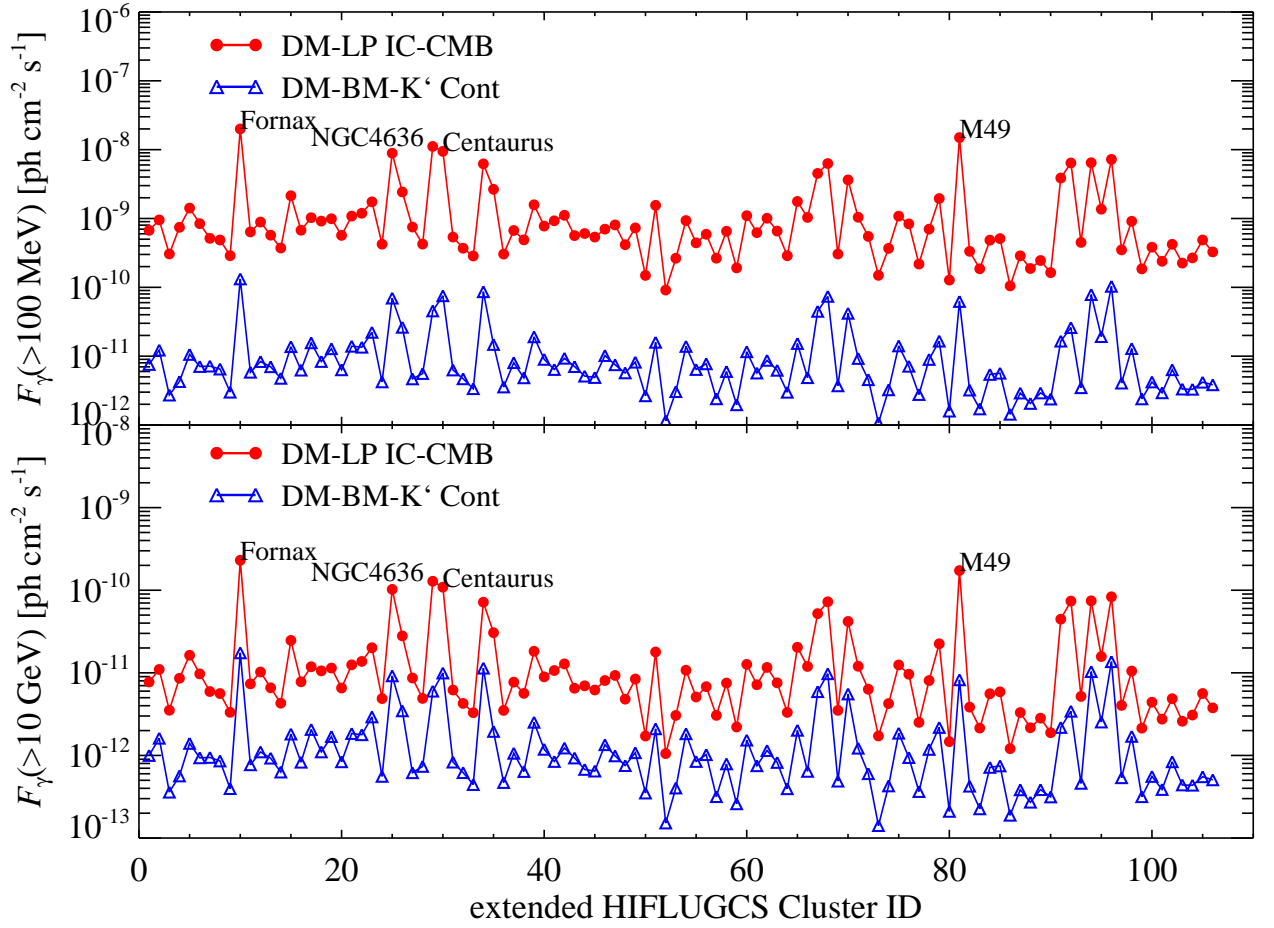


FIG. 20. Comparing the flux from clusters in the extended HIFLUGCS catalogue. We show the energy integrated gamma-ray fluxes derived from both leptophilic DM that result in inverse Compton upscattered CMB photons (red), and the continuum emission from the DM K' benchmark model (blue). The fluxes are calculated within r_{200} for each of the 106 clusters included in the extended HIFLUGCS catalogue, and are derived using a single beta profile for each cluster's gas density profile (see text for details). The upper panel show the energy integrated flux above 100 MeV and the lower panel above 10 GeV, both as a function of HIFLUGCS cluster ID. The name of the four brightest clusters are written out, where Fornax and M49 are the brightest targets.